



# Glacial retreat converts exposed landscapes from net carbon sinks to sources



A. J. Pain <sup>1,3</sup>, J. B. Martin <sup>2,3</sup>, E. E. Martin <sup>2</sup>, J. T. Salinas-Reyes <sup>2</sup> & C. Bennett<sup>2</sup>

Retreat of continental ice sheets exposes comminuted sediment in disequilibrium with non-glacial conditions. Weathering of this sediment may create climate feedbacks by altering exchange of greenhouse gases between atmosphere and landscapes. Here we show in a partially deglaciated watershed in southwest Greenland that glacial meltwater contains low concentrations of reactive dissolved organic carbon that enhances weathering of freshly comminuted sediment causing net sequestration of carbon dioxide. In contrast, soil water reactions enhance methanogenesis and carbon dioxide production and create greenhouse gas sources as organic carbon is remineralized. We suggest that a change from greenhouse gas sinks in glacial meltwater to greenhouse gas sources in soil water creates a switch from a negative to positive warming feedback during glacial-interglacial transitions, but a negative warming feedback may return with future anthropogenic warming, glacial retreat, and increased meltwater production. We anticipate changing weathering reactions following exposure also alter nutrient and radiogenic isotope exports.

Since the Pleistocene, continental ice sheets have periodically covered and retreated from ~30% of Earth's land surface with well-known effects on sea level<sup>1</sup> and global isostatic adjustments. In addition, retreating ice sheets expose fine-grained comminuted glacial sediment out of chemical equilibrium with environmental conditions that develop following deglaciation<sup>2</sup>, a concept similar to geomorphic disequilibrium of glacial sediment deposited in proglacial and paraglacial landscapes<sup>3–5</sup>. Chemical disequilibrium drives weathering reactions, which are intensified by global warming during glacial-interglacial transitions and more recently with anthropogenic climate change<sup>6–8</sup>. Recent anthropogenic warming has also increased glacial meltwater runoff<sup>9,10</sup>, which may impact solute and gas fluxes to the oceans and atmosphere. The potential impacts have led to multiple studies of the relationship between accelerated ice melt and glacial meltwater stream chemistry<sup>11–16</sup>. Although these studies reflect the role of glacial meltwater in global solute and greenhouse gas cycling, little is known of how disequilibrium and associated mineral weathering reactions alter solute and gas budgets following glacial retreat and exposure of deglaciated landscapes, i.e., those that were previously glaciated but are now exposed without hydrologic connections to ice sheet meltwater drainages<sup>2,17</sup>.

Streams draining deglaciated landscapes have received less attention than glacial meltwater streams in part because they have lower instantaneous discharge compared with meltwater streams. However, a comparison of discharge of the proglacial Akuliarusiaarsuup River which drains a portion

of the Greenland Ice Sheet across a landscape with dry desert like conditions with a nearby deglaciated coastal watershed with humid conditions indicates they have similar specific discharge (discharge normalized to drainage areas). Although the similarity in discharge of the two distinct streams results from a regional precipitation gradient, it implies deglaciated watersheds can represent sources of solutes to receiving waters such as the coastal ocean of similar importance to proglacial systems<sup>18</sup>. Vast regions of terrestrial landscapes are exposed during the loss of ice sheets, resulting in deglaciated watersheds exporting large volumes of water and solutes to the global ocean. For example, the Arctic Ocean, which contains ~1% of total ocean volume, receives ~10% of Earth's freshwater, mostly from streams draining Canadian and Siberian deglaciated watersheds<sup>19</sup>. Nutrient sources from deglaciated watersheds support approximately a third of Arctic Ocean productivity<sup>20,21</sup>. Consequently, the evolution of solute chemistry as weathering reactions approach equilibrium following exposure could play an important role in changing solute fluxes. Similarly, changes in weathering reactions as systems approach chemical equilibrium may also impact greenhouse gas exports, particularly CO<sub>2</sub> and CH<sub>4</sub>, thereby altering their effects on climate change.

How weathering reactions impact the global carbon cycle, and specifically their effects on atmospheric CO<sub>2</sub> concentrations, depends on both the mineral phases involved in the reactions and the acid causing the weathering (Supplementary Table 1)<sup>22,23</sup>. Associated changes in the global carbon cycle

<sup>1</sup>University of Maryland Center for Environmental Science, Horn Point Lab, Cambridge, MD, USA. <sup>2</sup>University of Florida Department of Geological Sciences, Gainesville, FL, USA. <sup>3</sup>These authors contributed equally: A. J. Pain, J. B. Martin. e-mail: [apain@umces.edu](mailto:apain@umces.edu)

provide a key control on global temperatures over geological timescales<sup>24,25</sup> and possibly shorter glacial-interglacial cycles<sup>22</sup>. While mineral weathering is an important sink of CO<sub>2</sub>, biogeochemical processes can produce both CO<sub>2</sub> and CH<sub>4</sub> through aerobic and anaerobic organic carbon (OC) remineralization reactions. Although CO<sub>2</sub> and CH<sub>4</sub> both contribute to greenhouse warming, CH<sub>4</sub> is a more potent greenhouse gas with roughly 25 times the warming potential of CO<sub>2</sub> over 100-year timescales and thus contributes disproportionately to greenhouse warming. For this reason, CH<sub>4</sub> fluxes are often reported in CO<sub>2</sub>-equivalents, which multiplies the flux of CH<sub>4</sub> by 25<sup>26</sup>. The amount of OC that can be remineralized, and thus the magnitude of CO<sub>2</sub> and/or CH<sub>4</sub> produced, depends on the quantity and quality of carbon substrates that govern the rate of gas production. Remineralization of these substrates is known to vary as a function of landscape exposure age following ice retreat. For instance, recently deglaciated landscapes have been shown to be dominated by relatively low amounts of microbially produced labile OC substrates that transition to more abundant stable humic and tannic OC substrates with ecosystem succession and soil development<sup>27-29</sup>. The transition in concentrations and qualities of soil OC also impacts OC delivery to streams and the ocean creating differences in stream<sup>30,31</sup> and coastal<sup>32</sup> ecosystem metabolism<sup>33,34</sup> as ice retreats.

Comparisons of exports from multiple deglaciated watersheds with distinct environmental characteristics have suggested that continued chemical weathering and soil development following exposure change solute and greenhouse gas production and consumption<sup>17,35</sup>. However, environmental characteristics, such as OC substrate concentrations and lability, vegetation communities, bedrock lithology, precipitation amounts, mean annual temperature, and temperature range, differ between the compared watersheds and confound interpretations of effects related to time since exposure by impacting weathering reactions and weathering products, OC remineralization, and carbon cycling. No previous study has compared greenhouse gas budgets in glacial and deglaciated portions of a single watershed characterized by consistent environmental conditions. Evaluating changes in stream chemistry in a single watershed, as done here, alleviates the complications related to variations in environmental characteristics between watersheds and thus would provide information about how greenhouse gas production and consumption, and linked fluxes between landscapes and atmosphere, will change with evolving

biogeochemical and weathering reactions due to exposure age. Initial biogeochemical reactions following exposure should enhance carbon fixation, increase microbial production of reactive nitrogen<sup>36-38</sup>, and release phosphorus and micronutrients from mineral reservoirs<sup>18,39</sup> while continued aging of the landscape should result in a shift towards OC remineralization that would produce CO<sub>2</sub> and CH<sub>4</sub>.

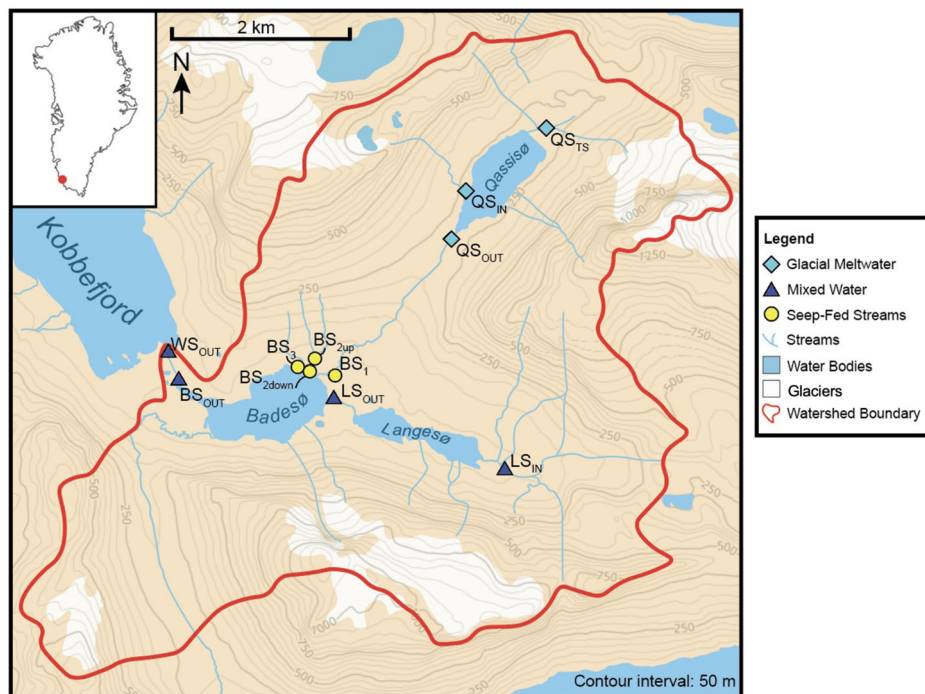
We hypothesize that magnitudes and pathways of CO<sub>2</sub> sequestration will diminish and CH<sub>4</sub> production will increase with the loss of glaciers as exposed comminuted sediments approach chemical equilibrium. We test this hypothesis with observations from a partially glaciated ~32 km<sup>2</sup> watershed that drains varying proportions of glacial meltwater and soil water in the active layer to Kobbefjord in southwest Greenland. Dominant water sources switch between glacial meltwater and soil water depending on temperature-controlled melting of the glaciers relative to continual seepage of soil water. We find that glacial meltwater is characterized by low OC concentrations with fluorescence characteristics suggesting elevated lability. In contrast, soil water has elevated OC concentrations comprised of more recalcitrant carbon. The more labile meltwater carbon is associated with rapid weathering of freshly comminuted glacial sediment. Weathering reaction mechanisms are identified through mass balance modeling of solute compositions that indicate net sequestration of CO<sub>2</sub> and CO<sub>2</sub> equivalents in glacial meltwater. In contrast, remineralization of more recalcitrant soil organic carbon under anaerobic conditions limits weathering loss of CO<sub>2</sub> and leads to a net source of CO<sub>2</sub> equivalents through CH<sub>4</sub> production. We discuss how these changes in reactions and the effects on solute and greenhouse gas concentrations may impact climate.

## Results and discussion

### Study location

We sampled streams draining to Kobbefjord, Greenland (Fig. 1) during two periods in July 2019. Sampled streams drain glacial meltwater and lake outlets, plus soil water sources that were collected from small seep-fed tributaries to the mainstream channels that lack any glacial meltwater (herein “seep-fed streams”; Supplementary Fig. 1). The underlying lithology of the Kobbefjord watershed is part of the Archean Block and is comprised of glacial sediments derived from underlying Eoarchean and Neoarchean terrains<sup>40</sup>. The climate of Kobbefjord is characterized as low-arctic polar

**Fig. 1 | Map of field site.** Discrimination of the various source waters is based on stable isotope values of the water and location of sampling site in the landscape.



tundra<sup>41</sup>. The Kobbefjord watershed was ice covered until ~10.7 ky ago, with more intense regional deglaciation between 9.1 and 7.9 ka, leaving small mountain glaciers covering ~1.7% of the watershed (Fig. 1)<sup>40,42,43</sup>. The current glaciers in the region are actively retreating and are predicted to last between 30–90 years based on current melt rates<sup>44</sup>. Current land cover consists of barren ground (32%), dry heath and grassland (29%), abrasion surfaces (19%), wet heath (17%), fen (2%), and copse and tall shrubs (1%)<sup>43</sup>. The glacial drainage flows through three lakes prior to being discharged to the fjord. Stream discharge during our study period was taken from the Greenland Ecosystem Monitoring database (<https://data.g-e-m.dk/>) as measured ~500 m upstream of the outlet to Kobbefjord and downstream of all lakes. On an annual average basis, ~8% of the watershed discharge originates as glacial meltwater but the magnitudes of water from various sources, including glaciers, soil water, lakes, and precipitation vary seasonally<sup>45</sup>. Peak outlet discharge lags peak snow and ice melt by ~8 h<sup>45</sup>.

### Inorganic mineral weathering reactions

Glacial meltwater mixes with seep-fed stream water as the primary streams flow through the tundra and lakes in the Kobbefjord watershed (Fig. 1). These two stream water sources can be separated based on their  $\delta^{18}\text{O}_{\text{H}_2\text{O}}$  and  $\delta\text{D}_{\text{H}_2\text{O}}$  values (Fig. 2), which vary systematically with their sampling locations. Isotope ratios are lowest in the headwater locations, where their dominate source is glacial meltwater. Isotope ratios are elevated in the seep-fed streams and exhibit enrichment in  $\delta^{18}\text{O}$  values compared with  $\delta\text{D}$  values relative to the meteoric water line, suggesting evaporative fractionation. Intermediate isotope values occur in lake outlet samples and in the downstream portions of the main channel, indicating mixing between the two endmembers. The  $\delta^{18}\text{O}$  values also show differing values and temporal patterns during two periods of high-resolution sampling at the watershed outlet (WS<sub>out</sub>, Fig. 3). Period 1 has significantly ( $p < 0.05$ ) lower  $\delta^{18}\text{O}_{\text{H}_2\text{O}}$  values than Period 2 (Fig. 4a) and exhibits diurnal variations that are lacking in Period 2 (Fig. 3). The low  $\delta^{18}\text{O}_{\text{H}_2\text{O}}$  values indicate a greater fraction of glacial meltwater in Period 1 compared with Period 2 and the diurnal variations correspond with diurnal variations in temperature and solar insolation leading to increased melting and glacial meltwater discharge. The increase in the source from seep fed stream water in Period 2 corresponds to significantly ( $p < 0.05$ ) less insolation, less variable and lower daily maximum temperature, and lower discharge than in Period 1 (Fig. 4b–d), consistent with lower glacial meltwater generation in Period 2 relative to soil and lake water sources. These differences, combined with water chemistry data and the results of mass balance estimates of mineral weathering, allow assessments of how glacial versus soil water sources may change riverine and landscape carbon dynamics. We proposed these changes serve as a microcosm of changes that occur during the loss of glacial ice from Arctic landscapes during glacial-interglacial transitions.

Offsets between co-occurring dissolved and bedload Sr isotopes ( $\Delta^{87}\text{Sr}^{86}\text{Sr}$ ) arise during initial weathering processes in streams draining glacial landscapes because of preferential leaching of loosely bound

radiogenic  $^{87}\text{Sr}$  from Rb-rich minerals, such as interlayer sites in biotite that is newly comminuted by glacial processes<sup>46</sup>. Previous work has demonstrated that preferential weathering of  $^{87}\text{Sr}$  produces elevated  $\Delta^{87}\text{Sr}^{86}\text{Sr}$  in recently exposed watersheds with dry climates compared to  $\Delta^{87}\text{Sr}^{86}\text{Sr}$  near equilibrium ( $= \sim 0$ ) in humid watersheds with older exposure ages, reflecting weathering of major rock-forming minerals that is approaching equilibrium<sup>17,35</sup>. In the small Kobbefjord watershed, where precipitation is spatially uniform,  $\Delta^{87}\text{Sr}^{86}\text{Sr}$  values will depend only on the time since mineral weathering began and the weathering environment, namely whether in soils (long weathering time) or draining from subglacial systems (short weathering time). Along with differences in time since exposure, differences occur between environments in the type of weathering acid (carbonic vs. sulfuric, Supplementary Table 1) and intensity of acid generation driving weathering. The significant ( $p < 0.01$ ) inverse relationship between  $\Delta^{87}\text{Sr}^{86}\text{Sr}$  and  $\delta^{18}\text{O}_{\text{H}_2\text{O}}$  values indicates weathering of  $^{87}\text{Sr}$  is closest to equilibrium in seep-fed streams (Fig. 5). The highest  $\Delta^{87}\text{Sr}^{86}\text{Sr}$  value occurs in a headwater sample of a glacial meltwater stream (QS<sub>TS</sub>) that also contains abundant fine grained, glacial rock flour (Supplementary Fig. 1a). The glacial meltwater streams also exhibit the greatest variability in  $\Delta^{87}\text{Sr}^{86}\text{Sr}$  with lower values in the cobble filled mountain stream (QS<sub>in</sub>) and lake outlet stream (QS<sub>out</sub>) that had insufficient fine-grained material to sample (Supplementary Fig. 1d). The  $\Delta^{87}\text{Sr}^{86}\text{Sr}$  values of mixed water samples fall between the turbid meltwater stream sample and all of the seep-fed streams. Changes in weathering environment defined by  $\Delta^{87}\text{Sr}^{86}\text{Sr}$  and  $\delta^{18}\text{O}_{\text{H}_2\text{O}}$  values correspond to exposure age, which for seep-fed stream sediment was ~10.7 ky ago, while glacial meltwater largely reacts with freshly exposed sediment.

While a regression between  $\delta^{18}\text{O}$  and  $\Delta^{87}\text{Sr}^{86}\text{Sr}$  values indicates a significant ( $p < 0.01$ ) linear relationship that reflects changes in mineral weathering extent across the watershed, systematic variations suggest that lakes may enhance mineral weathering. Additional in-lake weathering is indicated by  $\Delta^{87}\text{Sr}^{86}\text{Sr}$  values that plot above the regression line for samples collected at lake outlet sites (Fig. 5). The elevated  $\Delta^{87}\text{Sr}^{86}\text{Sr}$  values are similar to the QS<sub>TS</sub> stream where weathering reactions are farther out of equilibrium with respect to bedload sediments than the less turbid glacial meltwater stream (QS<sub>in</sub>) or the outlet of the proglacial lake (QS<sub>out</sub>). These deviations from the regression line suggest that mineral weathering is enhanced and produces higher values of  $\Delta^{87}\text{Sr}^{86}\text{Sr}$  in lake water where long residence times and strong acids produced by lake bottom sediments intensify mineral weathering reactions, including weathering of radiogenic micas that may become concentrated in lake sediment from settling in non-flowing water. Offsets from the trend in Fig. 5 reflect the important role lakes have in generation of reaction products from weathering processes.

Major solute concentrations and reaction stoichiometry (Supplementary Table 1), estimated from mass balance calculations (see Methods section), indicate relative amounts of inorganic weathering reaction mechanisms vary between glacial meltwater, seep-fed streams, and mixed waters and drive differences in  $\text{CO}_2$  sequestration due to mineral weathering

**Fig. 2 | Stable isotopic composition of water samples.** Samples are color coded by their putative sources including glacial meltwater streams (light blue), seep-fed streams (yellow), and mixtures of these two sources (dark blue). The dashed line represents the Global Meteoric Waters Line (GMWL) showing evaporative enrichments of  $\delta\text{D}_{\text{H}_2\text{O}}$  values in some of the seep-fed stream water.

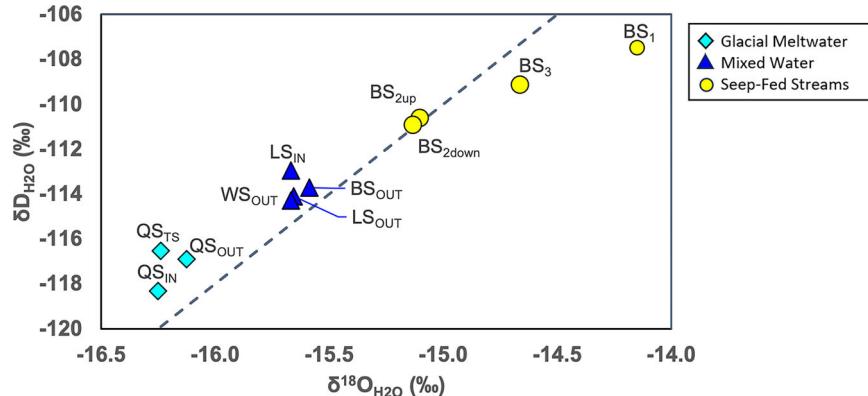


**Fig. 3 | Discharge, stable isotopes of water, and hydroclimatic variables over time.** Time series variations include stream discharge (black line), air temperature (blue line), and insolation (orange line) measured at 15 min intervals at Site BS<sub>out</sub>. Discharge and temperature data are from the GEM database (<https://g-e-m.dk/>); insolation values were measured during this project.  $\delta^{18}\text{O}_{\text{H}_2\text{O}}$  values (green symbols) for water samples were collected at three-hour frequency from the WS<sub>out</sub> site during Periods 1 and 2. Insolation values, peak temperatures, and discharge are higher in Period 1 than Period 2.

During Period 1,  $\delta^{18}\text{O}$  values show diurnal periodicity with elevated values corresponding to peak temperatures, indicating meltwater production with an ~8 h lag in discharge from glacier to watershed outlet identified by Abermann et al. (2021). During Period 2,  $\delta^{18}\text{O}$  values are higher, and although variable, do not show a systematic diurnal periodicity indicating smaller contributions of glacial meltwater compared with Period 1.

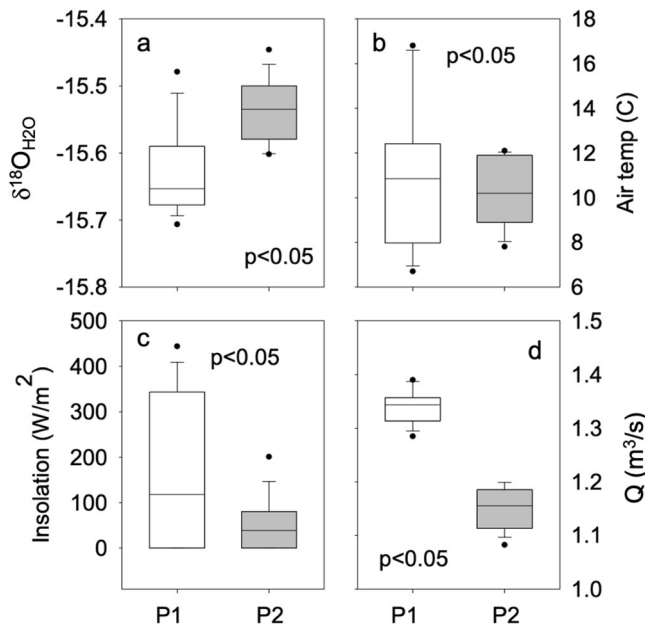
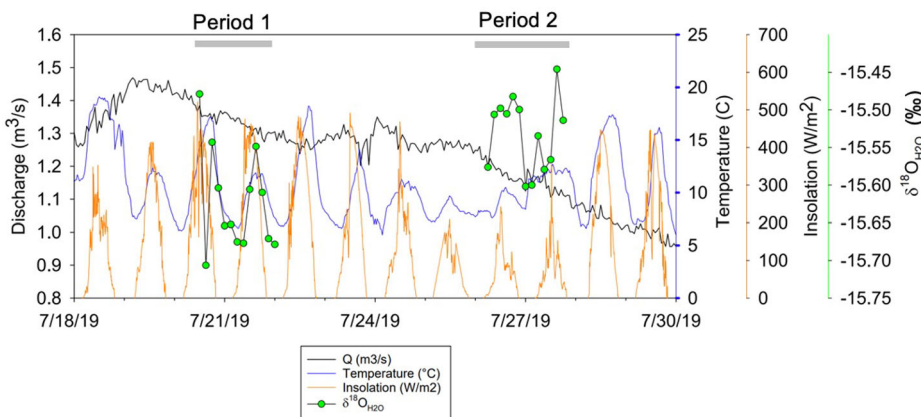


**Fig. 4 | Box plots of discharge, stable isotopes of water, and hydroclimatic variables between sampling periods.** Box and whisker plots of time series data from WS<sub>out</sub> during sampling Periods 1 (P1) and 2 (P2) and include a)  $\delta^{18}\text{O}_{\text{H}_2\text{O}}$  values b) air temperature, c) insolation, and d) discharge, with the bars representing mean values. The data show a significant decrease in mean temperature, insolation, and discharge values from Period 1 to Period 2, and a significant increase in the  $\delta^{18}\text{O}_{\text{H}_2\text{O}}$  values from Period 1 to Period 2. In addition, the range of both insolation and temperature is larger in Period 1 than Period 2.

(Fig. 6). Seep-fed stream water has more carbonic acid weathering of silicate minerals (CA<sub>sil</sub>) than mixed or glacial meltwater in contrast with glacial and mixed waters, which have more carbonic acid weathering of carbonate minerals (CA<sub>carb</sub>) than seep-fed stream water (Fig. 6a, b). Mixed water at lake outlets has more sulfuric acid weathering of both carbonate (SA<sub>carb</sub>) and silicate minerals (SA<sub>sil</sub>) than glacial and seep-fed stream water (Fig. 6c, d). The elevated weathering by sulfuric acid in lakes suggests production of sulfuric acid as sulfide diffuses from reducing lake sediment to oxic lake water, indicating one process whereby lakes impact watershed biogeochemical reactions<sup>47–49</sup>.

The distribution of reaction mechanisms shown in Fig. 6 and variations in  $\Delta^{87}\text{Sr}^{86}\text{Sr}$  values shown in Fig. 5 indicate weathering in glacial meltwater is dominated by reactive minerals such as carbonate and biotite in freshly comminuted sediment. In contrast, the greater fraction of silicate mineral weathering in seep-fed streams, and low  $\Delta^{87}\text{Sr}^{86}\text{Sr}$  values, reflects loss of reactive phases during weathering over longer exposure times following deglaciation and by additional weathering with sulfuric acid. Weathering of more recalcitrant, major rock-forming minerals is also limited in glacial meltwater by its short residence time in stream channels (~8 h) but could occur over long periods in soil water that source seep-fed streams. Glacial meltwater has colder temperature than soil water which increases solubility and weathering of carbonate minerals, enhancing its weathering. The distribution of distinct weathering reactions among the primary source waters and weathering environments suggests varying impacts on net CO<sub>2</sub> and CH<sub>4</sub> production and consumption.

#### Organic carbon remineralization and greenhouse gas production

Organic carbon remineralization is a primary reaction mechanism for production of CO<sub>2</sub> and CH<sub>4</sub>, although subsequent CO<sub>2</sub> hydration to carbonic acid drives mineral weathering reactions that sequester CO<sub>2</sub> as bicarbonate. Remineralization rates, and thus CO<sub>2</sub> and CH<sub>4</sub> production, depend on OC sources and reactivity. In the Kobbefjord watershed, OC quantity and quality depend on water source as reflected in the significant linear relationships between  $\delta^{18}\text{O}$  values and DOC concentrations ( $p < 0.001$ ), OC quality fluorescent and absorbance indices ( $p < 0.01$ ), and C/N ratios ( $p < 0.05$ ) (Fig. 7). Although glacial meltwater streams have lower DOC concentrations than seep-fed streams, the C/N ratios and spectroscopic indices (low SUVA<sub>254</sub>, high BIX, and low HIX values) indicate the DOC is more reactive than nonglacial water sources (Fig. 7b–e). In contrast, seep fed streams have elevated DOC concentrations and C/N ratios, and quality indices (high SUVA<sub>254</sub>, low BIX and high HIX values) that indicate high concentrations of recalcitrant structural molecules, such as lignin, from soil or terrestrial vegetation sources<sup>46,50</sup>. Thus, DOC associated with glacial meltwater is likely more bioavailable and readily remineralized to CO<sub>2</sub> and/or CH<sub>4</sub>, which would enhance weathering regardless of its lower concentrations than nonglacial sources.

Water sources have distinct CO<sub>2</sub> and CH<sub>4</sub> concentrations that vary systematically with their  $\delta^{18}\text{O}_{\text{H}_2\text{O}}$  values (Fig. 6e, f). Seep-fed stream water has CO<sub>2</sub> and CH<sub>4</sub> concentrations that are orders of magnitude greater than expected from equilibration with the atmosphere because of remineralization of organic-carbon rich soils. In contrast, both glacial meltwater and mixed samples are near equilibrium with atmospheric CO<sub>2</sub> and

**Fig. 5 |  $\delta^{18}\text{O}_{\text{H}_2\text{O}}$  of samples versus the difference between paired stream water and fine-grained bedload sediment  $^{87}\text{Sr}/^{86}\text{Sr}$  ( $\Delta^{87}\text{Sr}/^{86}\text{Sr}$ ). Due to a lack of fine-grained sediment at  $\text{QS}_{\text{in}}$ ,  $\text{LS}_{\text{out}}$ , and  $\text{WS}_{\text{out}}$  (Supplementary Fig. 2d),  $\Delta^{87}\text{Sr}/^{86}\text{Sr}$  was calculated using  $^{87}\text{Sr}/^{86}\text{Sr}$  values from proximal bedload samples. The dashed line is a linear regression showing a significant inverse relationship interpreted to reflect preferential weathering of radiogenic  $^{87}\text{Sr}$  in glacial meltwater compared with weathering closer to equilibrium ( $\Delta^{87}\text{Sr}/^{86}\text{Sr}$  ratio approaching zero) in the seep-fed streams. Bedrock lithologies vary across the watershed, but stream waters interact with moraine sediments homogenized by glacial processes alleviated bedrock age differences. In addition, the interpretation of weathering extent is based on the offset between stream water and bedload  $^{87}\text{Sr}/^{86}\text{Sr}$  rather than absolute values.**

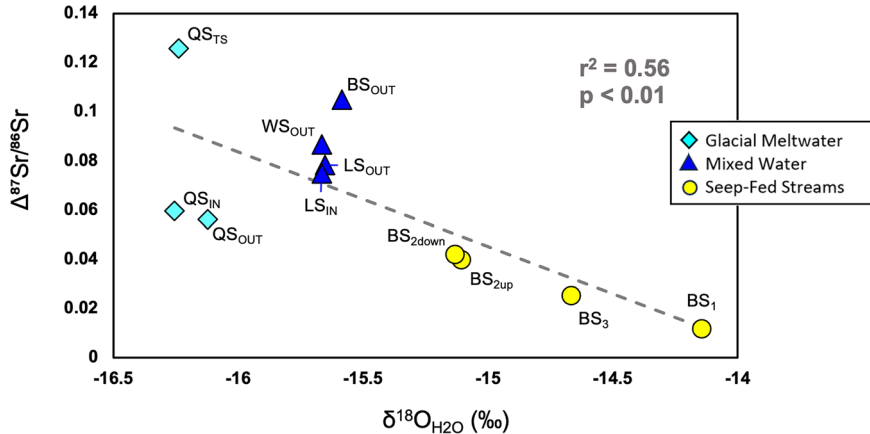
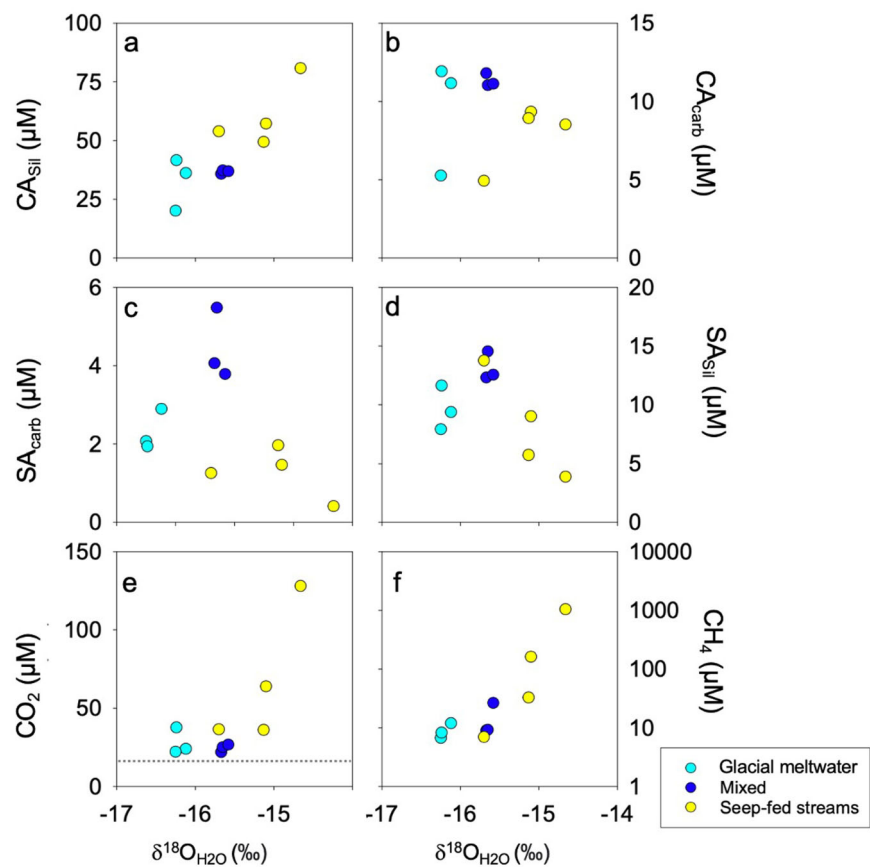


**Fig. 6 | Absolute values of  $\text{CO}_2$  consumption or production by distinct mineral weathering reactions versus  $\delta^{18}\text{O}_{\text{H}_2\text{O}}$ .** Mineral weathering reactions include (a)  $\text{CA}_{\text{sil}}$ , (b)  $\text{CA}_{\text{carb}}$ , (c)  $\text{SA}_{\text{carb}}$ , (d)  $\text{SA}_{\text{sil}}$  and variations in greenhouse gas concentrations include (e)  $\text{CO}_2$ , and (f)  $\text{CH}_4$ . Atmospheric equilibrium concentrations of  $\text{CO}_2$  is given by dashed grey lines ( $\sim 14 \mu\text{M}$ ), while this value is below  $1 \mu\text{M}$  for  $\text{CH}_4$ .  $\text{SA}_{\text{carb}}$ ,  $\text{CA}_{\text{sil}}$ , and  $\text{CA}_{\text{carb}}$  are expressed in terms of the absolute value of the impact on  $\text{CO}_2$  while  $\text{SA}_{\text{sil}}$ , which has no impact on  $\text{CO}_2$ , is expressed in moles of reaction<sub>2</sub>. Source waters include glacial meltwater streams (light blue), seep-fed streams (yellow), and mixtures of these two sources (dark blue).



slightly elevated above equilibrium with atmospheric  $\text{CH}_4$ . Although  $\text{CH}_4$  sources occur in some subglacial settings<sup>47,51</sup> and may act as an atmospheric source, distributions of  $\text{CO}_2$  and  $\text{CH}_4$  concentrations across the Kobbefjord watershed indicate that greenhouse gas fluxes to the atmosphere are greater in the seep-fed than glacial meltwater streams. Although soil water provides both baseflow water and dissolved gases to streams in deglaciated watersheds<sup>48,49,52,53</sup>, gas concentrations near atmospheric equilibrium in some Kobbefjord seep-fed streams and all mixed samples indicate some of the produced greenhouse gas evades to the atmosphere prior to discharge to streams. Our estimates of whole watershed gas exports described below and based on concentrations at the

watershed outlet, do not include this evasion and thus underestimate whole watershed greenhouse gas fluxes.

#### Watershed solute and dissolved gas exports

Time series sampling at the watershed outlet shows significantly ( $p < 0.05$  for  $\text{CO}_2$ ;  $p < 0.0001$  for  $\text{CH}_4$ ) lower  $\text{CO}_2$  and  $\text{CH}_4$  concentrations in Period 1 compared with Period 2 (Fig. 8a, b). These lower gas concentrations result from a larger fraction of  $\text{CO}_2$ - and  $\text{CH}_4$ -depleted glacial meltwater during Period 1 (Fig. 4a). During Period 1, sulfuric acid weathering of carbonate minerals ( $\text{SA}_{\text{carb}}$ ) produces more  $\text{CO}_2$  and carbonic acid weathering of carbonate minerals ( $\text{CA}_{\text{carb}}$ ) consumes more  $\text{CO}_2$  compared with Period 2

**Fig. 7 |  $\delta^{18}\text{O}_{\text{H}_2\text{O}}$  values versus dissolved organic concentrations and quality indices.** Included are (a) dissolved organic carbon (DOC), reflecting greater DOC concentrations in active layer water than glacial meltwater and  $\delta^{18}\text{O}_{\text{H}_2\text{O}}$  values versus dissolved organic matter (DOM) quality indicators including (b) molar C/N ratios of dissolved organic matter, (c) SUVA<sub>254</sub>, (d) BIX, and (e) HIX. The dashed lines represent in b) approximate C/N values for terrestrial and algal/microbial DOM, in (d) approximate BIX boundary separating autochthonous, non-degraded DOM from allochthonous degraded DOM, and in (e) the approximate values of HIX for soil and fresh DOM (Supplementary Table 2). The significant positive linear relationships in panels b, c, and e and negative relationship in panel d reflect the presence of more labile and less degraded DOM in glacial meltwater than seep-fed stream water. Orange arrows indicate the change in values toward more reactive DOC in panels b, c, d, and e.

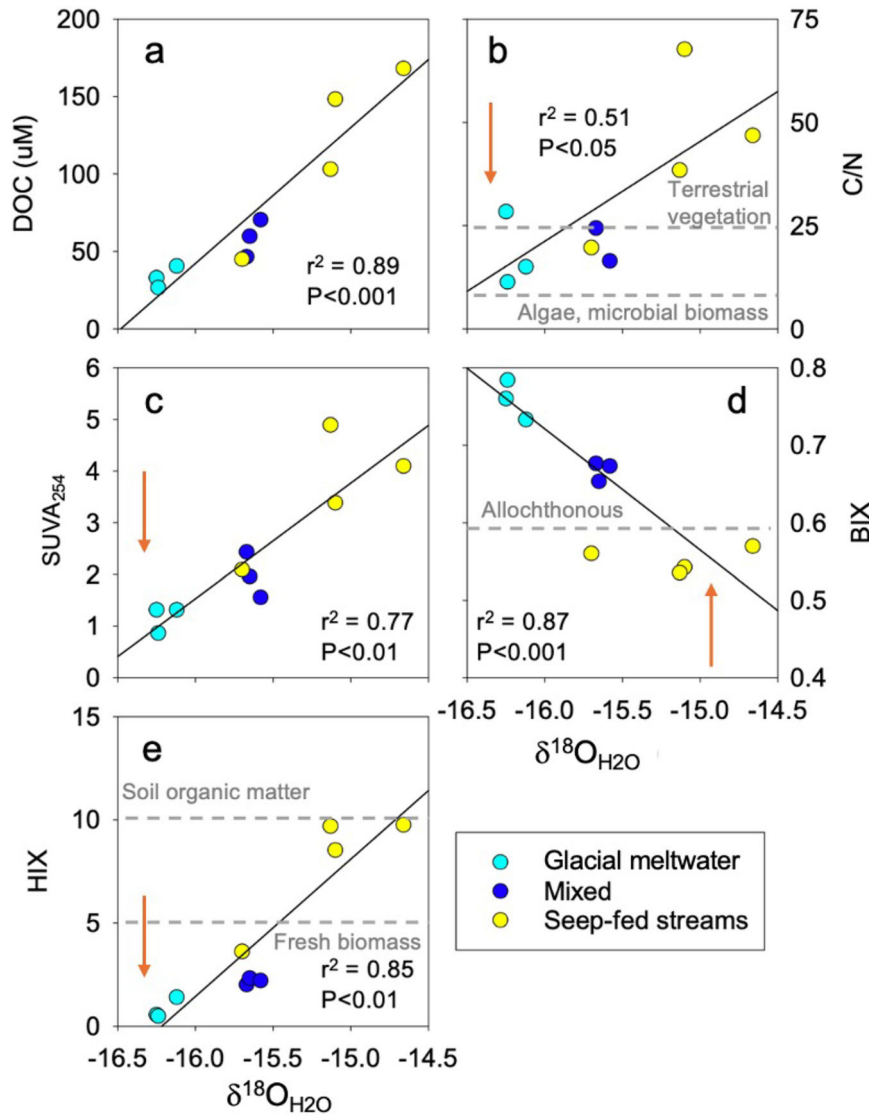


(Fig. 8c, e). In contrast, during Period 2, carbonic acid weathering of silicate minerals ( $\text{CA}_{\text{sil}}$ ) consumes more  $\text{CO}_2$  than in Period 1 (Fig. 8d). Increased weathering consumption of  $\text{CO}_2$  from Period 1 to Period 2 is shown by a smaller increase in mean  $\text{CO}_2$  concentrations (10% greater) compared with the increase in  $\text{CH}_4$  concentrations (415% greater), although both gases are derived from organic carbon remineralization (Fig. 8a, b).

Despite variation in DOC concentrations between glacier meltwater, lake outlet, and seep-fed stream sources (Fig. 7a), the watershed outlet sampled during Periods 1 and 2 shows no significant changes in DOC concentration between periods (Fig. 8f), regardless of shifts in the primary source water of the time-series samples. The similarity in outlet DOC concentrations between sample periods implies DOC concentrations are altered by in-stream biogeochemical processes that overprint variations in source water DOC concentrations. These processes would depend on delivery of both reactive OC and nutrients to the stream, which would simultaneously fuel primary productivity and heterotrophic remineralization, thereby altering both the total pool and reactivity of the stream water DOC.

We further evaluate possible in-stream processes leading to homogenization of DOC by estimating its export and quality during the two time-series sampling periods. We determine the DOC mass discharge at the stream outlet and average DOC exports during both sampling periods by multiplying instantaneous stream discharge with the corresponding DOC concentrations (Fig. 9). In addition, we use DOC quality indices to evaluate

reactivity, and thus putative in-stream modification of the exported DOC. Although glacial meltwater has DOC concentrations that are ~2 to 3 times lower than the nonglacial water sources (Fig. 7a), the higher discharge in Period 1 than Period 2 causes significantly ( $p < 0.05$ ) greater export of DOC in Period 1 compared with Period 2 (Fig. 9a). However, most DOC quality indices were not significantly different between Period 1 and Period 2 except for significantly lower BIX values ( $p < 0.05$ ) in Period 1 (Supplementary Fig. 2). Contrary to expectations, this difference in BIX values suggests that DOC exported during Period 2 has a more autochthonous signal and thus may be more labile than the DOC exported during Period 1, reflecting possible overprinting of in-stream or lake processes of signals expected from the increase in recalcitrant seep water DOC. In-stream and lake processes could be fueled by increased contribution of seep-fed streams in Period 2 which would be expected to be enriched in remineralized nutrients that could fuel metabolism of stream microbial communities and subaquatic vegetation<sup>48</sup>. Such in-stream processing of DOC complicates estimates of glacial and nonglacial DOC exports, the quality of these DOC exports, and their potential impact on coastal ecosystems<sup>27</sup>.

To determine the instantaneous  $\text{CO}_2$  and  $\text{CH}_4$  mass discharge at the stream outlet, we multiply stream discharge by dissolved gas concentrations and moles of each mineral weathering reaction type ( $\text{CA}_{\text{carb}}$ ,  $\text{CA}_{\text{sil}}$ , and  $\text{SA}_{\text{carb}}$ ) in the time series samples (Fig. 9). We express the  $\text{CH}_4$  mass discharge in terms of  $\text{CO}_2$  equivalents ( $\text{CH}_4\text{-CO}_{2\text{eq}}$ ) where 1 mole of  $\text{CH}_4$  has 25 times the potential warming as 1 mole of  $\text{CO}_2$ . The  $\text{CA}_{\text{carb}}$ ,  $\text{CA}_{\text{sil}}$ , and

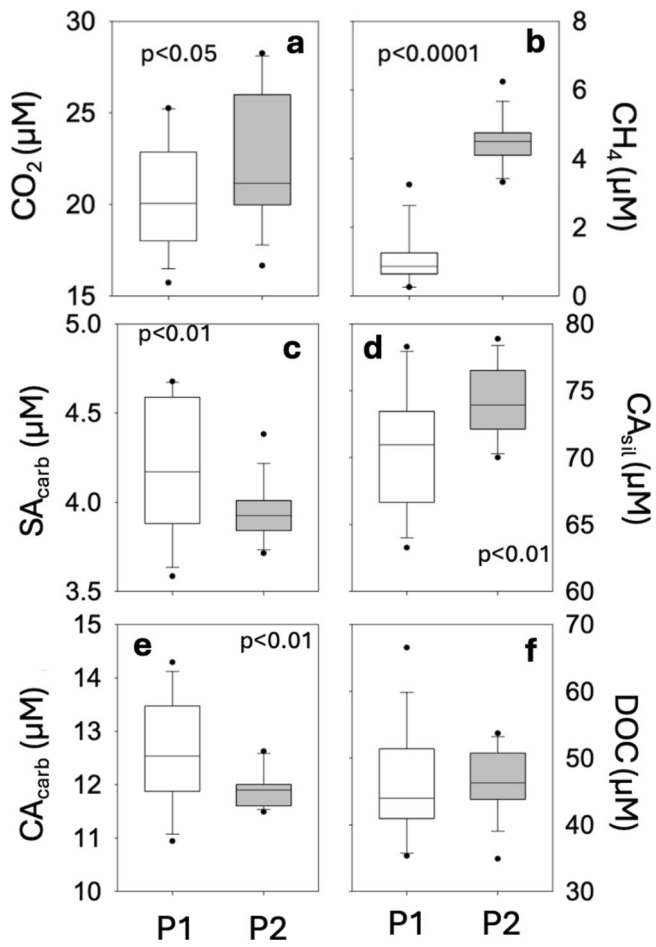


**Fig. 8 | Box plots of gas concentrations and mineral weathering products between sampling periods.** Measurements were made at the watershed outlet stream ( $WS_{out}$ ) during Period 1 (P1) and Period 2 (P2). Greenhouse gas concentrations include (a)  $CO_2$  and (b)  $CH_4$  concentrations. Weathering reactions include (c)  $SA_{carb}$ , (d)  $CA_{sil}$ , (e)  $CA_{carb}$ , and (f) DOC (Supplementary Table 1).  $SA_{carb}$ ,  $CA_{sil}$ , and  $CA_{carb}$  are expressed in terms of the absolute value of the impact on  $CO_2$ .

$SA_{carb}$  values are reported as the molar impact of each reaction on  $CO_2$  concentrations at the watershed outlet (Fig. 9d-f). The estimated mass discharge indicates how riverine greenhouse gas exports shift from Period 1 to Period 2 as proportions of glacial meltwater decrease relative to seepage water. Although both gases have significantly greater concentrations at the outlet during Period 2 compared with Period 1 (Fig. 8a, b), greater discharge during Period 1 than Period 2 results in no significant difference in mass discharge of  $CO_2$  (Fig. 9b). In contrast,  $CH_4$ - $CO_{2eq}$  discharge is 3.5 times greater during Period 2 than Period 1 (Fig. 9c).

We estimate  $CO_2$  equivalent atmospheric exchange ( $CO_{2eq(ex)}$ ) for discharge at the watershed outlet for both Period 1 and Period 2 according to

$$CO_{2eq(ex)} = CO_{2(aq)} + CH_4 - CO_{2eq(aq)} + C_{Acarb} + C_{Asil} \quad (1)$$

where  $CO_{2(aq)}$  is the hydrologic export based on aqueous  $CO_2$  concentrations (positive),  $CH_4$ - $CO_{2eq(aq)}$  is the hydrologic export based on aqueous  $CH_4$  concentrations stated as  $CO_2$  equivalents (positive), and  $CA_{carb}$  and  $CA_{sil}$  represents consumption of  $CO_2$  by carbonic acid weathering of carbonate and silicate minerals (negative) within the watershed (Fig. 10a). The  $CO_2$  provided by sulfuric acid weathering of carbonate minerals ( $SA_{carb}$ ) within the watershed makes up a portion of the  $CO_{2(aq)}$  term and thus is not explicitly included in Eq. 1. Thus,  $CO_{2eq(ex)}$  represents the potential integrated atmospheric exchange of  $CO_2$  and  $CH_4$  estimated from the hydrologic export during flow through and weathering within the watershed.

Summing these instantaneous reaction amounts (Fig. 10b) shows Period 1 has an average negative  $CO_{2eq(ex)}$  value of  $-64.5 \pm 27.7$  mmol  $CO_{2(ex)}$   $s^{-1}$ , providing a net sink of greenhouse gases. This sink is dominated by silicate mineral weathering by carbonic acid, which is expected during Period 1 when fine grained, freshly comminuted sediments react rapidly in glacial source water. Enhancing these weathering reactions is the presence of labile DOC in glacial source water (Fig. 7) that would rapidly remineralize to  $CO_2$  when exposed to atmospheric oxygen and subsequently hydrate to carbonic acid. In contrast, summing instantaneous reactions shows Period 2 has a positive average  $CO_{2eq(ex)}$  value of  $44.0 \pm 19.6$  mmol  $CO_{2(ex)}$   $s^{-1}$ , because of increased contributions of  $CH_4$  in soil seep waters from methanogenesis and slight decreases in carbonic acid mineral weathering in old, reacted soil sediments close to chemical equilibrium (Fig. 6f).

We convert our estimates of carbon estimates to mass units on an annual basis for comparison with previous similar estimates. The conversion indicates  $CO_2$  equivalent atmospheric exchange vary from  $-22 \pm 10$  Mg  $Cyr^{-1}$  in Period 1 to  $+18 \pm 7$  Mg  $Cyr^{-1}$  in Period 2, which are small, but within the range of riverine  $CO_2$  export reported elsewhere<sup>54</sup>. However, estimates of yearly exchange are complicated by seasonal variations in mineral weathering reactions, organic carbon processing, and proportions of water delivered to the outlet stream from various sources in a partially glaciated watershed. Especially important, our estimates lack observations during freshet when snow melt dominates discharge and flushes soil water that reacted over winter and would be expected to increase the positive atmospheric exchange. The importance of freshet sampling is highlighted by a maximum annual discharge rate of  $3.5 \text{ m}^3 \text{ s}^{-1}$ <sup>45</sup>, which is more than twice the highest discharge rate during our sampling. The lack of freshet sampling is a common problem and remains a critical unknown in evaluating annual exports from Arctic landscapes<sup>55</sup>.

Our extrapolations to yearly exports thus have large uncertainties and emphasize that improved estimates of annual greenhouse gas exchange require sampling across the range of discharge throughout the melt season. Nonetheless, our two sampling periods provide insight into how hydroclimatic shifts ranging from seasonal to glacial-interglacial timescales may affect riverine greenhouse gas exchange. Our results show riverine greenhouse gas budgets are sensitive to shifts in water sources between glacial and seep-fed streams because of environmental differences in greenhouse gas sources associated with OC remineralization and inorganic mineral weathering. Even small variations in water sources change the magnitude and sign of greenhouse gas export within the Kobbefjord watershed and suggest similar shifts in OC remineralization and weathering occur as glacial-interglacial transitions expose large areas of Earth's land surface.

### Implications for weathering feedbacks to warming

The ~30% of the Northern Hemisphere exposed by retreating ice sheets since the Last Glacial Maximum<sup>2</sup> has produced a shift in the proportion of glacial and proglacial watershed relative to deglaciated drainages<sup>56</sup>. Our results indicate that weathering of fresh comminuted sediment would dominate in glacial meltwater during glacial to interglacial transitions, resulting in net  $CO_2$  sinks, as exemplified by Period 1 sampling (Fig. 10b). In contrast, deglaciated landscapes that form OC rich soils are sites of biogeochemical reactions with more mature weathering that enhances  $CO_2$  and  $CH_4$  production and limits  $CO_2$  consumption. These results are consistent with previous studies of shifts in mineral weathering and impacts to Sr isotope exports, but which were complicated by differences in environmental conditions across broad study areas. For example, the extent of weathering has been shown to cause  $\Delta^{87}Sr/^{86}Sr$  values to decrease from ~0.05 to ~0 across an ~200 km transect in Southwest Greenland in watersheds with increasing exposure age (from ~7 to 10.4 ka)<sup>17</sup>. The change in  $\Delta^{87}Sr/^{86}Sr$  values across multiple watersheds is similar to the change in Sr isotope ratios in this study, although we find  $\Delta^{87}Sr/^{86}Sr$  as high as ~0.12 in glacial meltwater containing suspended sediment that has experienced essentially no prior weathering. Similarly, watersheds with longer exposure ages that have low  $\Delta^{87}Sr/^{86}Sr$  values reflecting increased mineral weathering have elevated

**Fig. 9 | Box plots comparing solute export in watershed outlet stream between sampling periods.** Measurements were made at the watershed outlet stream ( $WS_{out}$ ) during Period 1 (P1) and Period 2 (P2). Included are (a) DOC, (b)  $CO_2$ , (c)  $CH_4-CO_{2eq}$ , (d)  $SA_{carb}$ , (e)  $CA_{sil}$ , and (f)  $CA_{carb}$ .

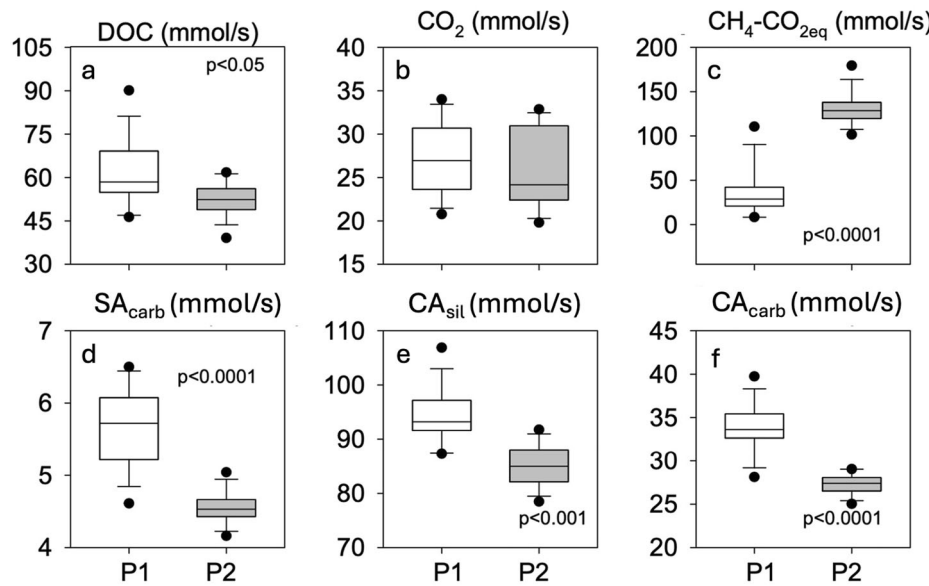
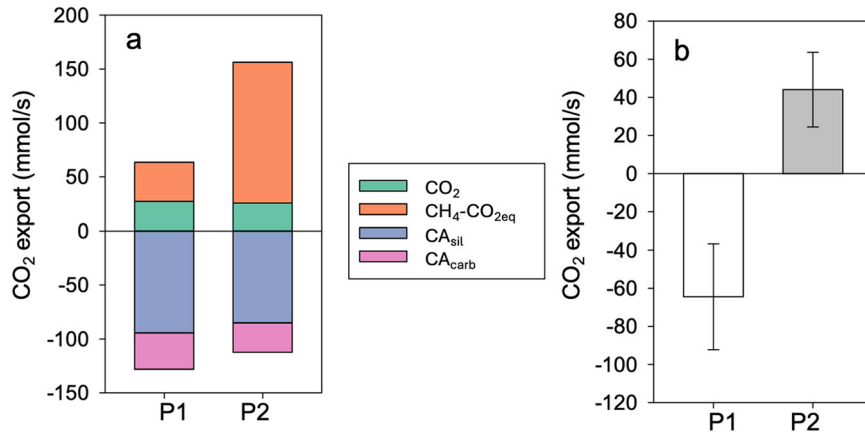


**Fig. 10 | Comparison of equivalent atmospheric gas exchange ( $CO_{2eq(ex)}$ ) between sampling periods.** Measurements were made at the watershed outlet stream ( $WS_{out}$ ) during Period 1 (P1) and Period 2 (P2). Included are (a) Gas exchange divided by processes, (b) Sum of net  $CO_2$  exports with uncertainty given by Eq. 1 showing a net sink of  $CO_2$  in P1 and net source of  $CO_2$  in P2.



DOC concentrations with quality indices indicating diminished lability. The similarity in DOC processing and mineral weathering across multiple watersheds with varying environmental conditions and within a single watershed indicate our findings of weathering and greenhouse gas cycling are applicable to all regions that have experienced loss of glacial ice. Specifically, our results suggest that greenhouse gas evasion from landscapes to the atmosphere will increase with the loss of glacial ice, such as during glacial-interglacial transitions, in response to changing reactive suspended sediment fluxes and biogeochemical processing of organic carbon substrates.

Changing riverine and soil water biogeochemical reactions should also impact timing and magnitude of other solute exports during glacial to interglacial transitions. Solutes that could be impacted include C, N, P, Si, and micronutrients<sup>18,27</sup> as well as the radiogenic isotopes of Nd and Pb. Changes in these isotope exports, which are suggested by variations in  $\Delta^{87}Sr/\Delta^{86}Sr$  values, are key in evaluations of changes in weathering during deglaciations as interpreted from their records in deep sea sediment deposits<sup>57–61</sup>. As weathering reactions approach equilibrium and greenhouse gas production is enhanced, our observations suggest greenhouse gas exports switch from net sequestration to net source. The timescales and magnitudes of shifts in greenhouse gas exchange depend on multiple factors including bedrock lithology of exposed landscapes and thus sediment reactivity, generation of nutrients and rate of organic soil development, and biogeochemical and hydrological characteristics that control redox

conditions and carbon cycling in developing soils. Nonetheless, our data suggest a shift in greenhouse gas exchange produces a change from a negative to positive feedback associated with global warming during glacial-interglacial transitions. However, rapid anthropogenic warming may increase glacial meltwater runoff in the short term, leading to a negative feedback on global warming.

## Methods

### Field area and sample sites

Stream water and sediment bedload samples were collected July 18 – 28, 2019 from various locations in a single 32.2 km<sup>2</sup> watershed referred to as Watershed 650 by Abermann et al.<sup>51</sup> that drains to Kobbefjord in southwestern Greenland (Supplementary Fig. 1). Prior to sample collection, in situ physicochemical water parameters were measured with a handheld meter. Landcover of the Kobbefjord watershed consists of barren ground (32%), dry heath and grassland (29%), abrasion surfaces (19%), wet heath (17%), fen (2%), and copse and tall shrubs (1%)<sup>43</sup>. Meltwater is supplied by mountain glaciers covering ~1.7% of the watershed. Glacial meltwater flows through two primary stream channels, both of which discharge to Badesø, the primary outlet lake (Supplementary Fig. 1c). Two other lakes, Qassisø and Langsø are within subwatersheds drained by the two primary stream channels. Glacial meltwater stream discharge is enhanced by tributaries disconnected from the ice sheet that drain soil water to seep-fed streams (Supplementary

Fig. 1b). Air temperature and insolation values were taken from the Greenland Ecosystem Monitoring database (<https://data.g-e-m.dk>).

Samples of water and sediment were collected once from 11 sites around the watershed. The sample sites include locations assumed to provide two putative end-member water sources: glacial meltwater and soil water seeping to streams (Supplementary Fig. 2a, b, d). Additional samples were collected from lake outlets and from downstream portions of the main channel near the outlet to Kobbefjord (Supplementary Fig. 1c), which were assumed to contain mixtures of glacier meltwater and soil water seeping to the streams and lakes. One sample site (WS<sub>out</sub>), near the watershed outlet to Kobbefjord, was sampled during two 36-hr time series, providing 29 samples that were collected at a 3-hr periodicity. The time series samples were collected on clear days July 20–22, 2019 (Period 1) and during cloudy days July 26–28, 2019 (Period 2). Bedload sediment was collected by hand using Ziplock bags at the same locations as the water samples except for three locations that were underlain by bedrock and/or cobbles and lacked small grain sized sediment (QS<sub>in</sub>, LS<sub>out</sub>, and WS<sub>out</sub>; Supplementary Fig. 1d). Care was taken to limit grain size fractionation of the sediment while sampling.

### Water sampling methodology

Water samples were collected using flexible PVC tubing placed in the main flow of the stream. The water was pumped into an overflow cup in which a YSI ProPlus sonde was installed. The sonde, which was calibrated daily, was used to monitor temperature (T), specific conductivity (SpC; electrical conductivity normalized to 25 °C), pH, and dissolved oxygen (DO) concentration and saturation. The parameters were monitored until they stabilized after which gas and water samples were collected using a variety of methods, preservatives, and sample bottles.

Gas, including both CO<sub>2</sub> and CH<sub>4</sub>, was separated from water aliquots using the headspace extraction method<sup>62,63</sup>. Unfiltered water was pumped into a 500 ml PVC bottle to overflowing. After slowly extracting the tubing while maintaining a meniscus at the bottle lip, the bottles were capped with rubber stoppers fitted with two short pieces of hard PVC tubing penetrating the stopper, each of which was attached to three-way gas-tight valves. The valves were used to extract 60 ml of water while simultaneously injecting ultrapure N<sub>2</sub> gas to fill the forming headspace. The headspace N<sub>2</sub> was equilibrated with dissolved gases in the sample by vigorous shaking for two minutes. Following equilibration, the headspace gas was extracted from the bottle through one of the three-way valves ensuring no atmospheric contamination. The extracted gas was immediately injected with a hypodermic needle through rubber septa into 60 ml glass serum bottles that were evacuated in the field immediately prior to storing the gas samples. Gas samples were returned to a US-based laboratory for analyses within 2 months of collection.

After gas sampling, the tubing was fitted with a 0.45 µm high-capacity trace metal grade canister filter and filtered water was pumped into sample bottles that had specific characteristics for preservation of each analyte. Samples for water stable isotope ratios (δD<sub>H2O</sub> and δ<sup>18</sup>O<sub>H2O</sub>) were collected in 2 ml glass vials that were filled to overflowing and sealed with screw cap lids without preservatives. For solute concentration samples, bottles and caps were rinsed three times with filtered sample water prior to filling. Cation and trace metal samples were collected in 20 ml prewashed (10% trace metal grade HNO<sub>3</sub>) HDPE bottles and preserved with Optima grade HNO<sub>3</sub> to pH < 2. Anion samples were collected with no preservative in 20 ml prewashed (18 MΩm DI water) HDPE bottles. Samples for chromophoric dissolved organic matter (CDOM), dissolved organic carbon (DOC), and total dissolved nitrogen (TDN) concentrations were collected in amber borosilicate vials that were combusted at 550 °C prior to use. The DOC and TDN samples were acidified with hydrochloric acid to pH < 2 while no preservative was added to CDOM samples. Samples for dissolved inorganic nitrogen (DIN), taken as the sum of nitrate + nitrite (NO<sub>3</sub> + NO<sub>2</sub>) and ammonium (NH<sub>4</sub>), were filtered directly into polypropylene vials with no preservative and frozen until analysis. All other water samples were chilled at 4 °C until analysis in US-based laboratories within 2 months of collection.

### Stream discharge

Stream discharge measurements were collected by Asiaq Greenland Survey (Nuuk, Greenland) as part of the Greenland Ecosystem Monitoring Programme (<https://g-e-m.dk>). Details on the stream discharge collection methods can be found in Abermann et al.<sup>45</sup>.

### Water isotope analyses

Water isotopes (δD<sub>H2O</sub> and δ<sup>18</sup>O<sub>H2O</sub>) were measured using a Picarro L2120-I cavity ring-down spectrometer coupled with a Picarro A0211 High Precision Vaporizer and a CTC HTS PAL autosampler. The results were calibrated with two internal University of Florida water standards: UW Antarctic water, with δD<sub>H2O</sub> and δ<sup>18</sup>O<sub>H2O</sub> values of -289.89 and -36.13‰, respectively, and Lake Tulane water with δD<sub>H2O</sub> and δ<sup>18</sup>O<sub>H2O</sub> values of 0.94 and 0.26‰ respectively. Precision was determined on 10 replicate samples yielding standard deviation of δ<sup>18</sup>O<sub>H2O</sub> = 0.09‰ and δD<sub>H2O</sub> = 0.41‰. All isotope results are reported in standard delta notation relative to Vienna Standard Mean Ocean Water (VSMOW).

### Sr separation and isotope analyses

For analyses of dissolved Sr isotope ratios, 25–100 ml of stream water containing ~200 ng of Sr was dried in acid-washed Teflon beakers. To remove organic matter, 250 µl concentrated Optima HNO<sub>3</sub> was added and dried twice. The sample was redissolved in 50 µl 1 N Optima HCl and processed through 0.5 ml columns loaded with BioRad AG50W-X8 cation exchange resin to remove Rb. The Sr fraction from these columns was further purified using Eichrom Sr-Spec resin according to standard column chemistry procedures<sup>64</sup>. For analyses of bedload Sr isotope ratios, a 3 g split of each bedload sediment sample was crushed with mortar and pestle and heated to 550 °C for 4 h in a muffle furnace to remove organic matter. Weight loss during heating was <1%. Approximately 0.05 g of the organic-free sample was weighed into 6 ml Teflon beakers and dissolved on a hotplate in a 3:1 mixture of concentrated Optima HF and HNO<sub>3</sub>. Once the sediment was dissolved, the solutions were dried down and sequentially treated and dried in Optima HNO<sub>3</sub> and HCl to breakdown and convert fluorides to chlorides in preparation for column chemistry. Rb and other cations were removed using primary columns packed with Biorad AG50W-X12 (200-400 mesh) cation exchange resin. The Sr cut from this column was also purified using Eichrom Sr-Spec resin<sup>64</sup>. The prepared water and bedload Sr fractions were analyzed for <sup>87</sup>Sr/<sup>86</sup>Sr ratios using wet plasma and time resolved analysis (TRA<sup>65</sup>) on a Nu Plasma multi-collector inductively coupled plasma mass spectrometer (MC-ICPMS). All analyses used on-peak zeros measured on unspiked 2% HNO<sub>3</sub> to correct for isobaric interferences from Kr impurities in the Ar carrier gas. Each sample was corrected for mass-bias using <sup>86</sup>Sr/<sup>88</sup>Sr = 0.1194 and <sup>87</sup>Sr was corrected for interference of <sup>87</sup>Rb. The NBS 987 standard was measured every 5–6 samples. The long-term average <sup>87</sup>Sr/<sup>86</sup>Sr value of TRA-measurements of NBS 987 at UF is 0.710246 (± 0.000030, 2σ). Procedural blanks were less than 100 pg Sr, which is three (waters) to seven (bedload) orders of magnitude less than sample Sr abundances.

### CO<sub>2</sub> and CH<sub>4</sub> analyses

Gas samples were simultaneously measured for their CO<sub>2</sub> and CH<sub>4</sub> concentrations using a Picarro G2201-I cavity ring-down spectrometer. Check standards were run and accurate to within 10% of reported values.

### Solute analyses

Major anion and cation concentrations were measured on automated Dionex ICS-2100 and ICS-1600 ion chromatographs, respectively, which were standardized with commercially available multi-element standards. Error on replicates was less than 5%. Concentrations of the components of DIN (NO<sub>3</sub> + NO<sub>2</sub> and NH<sub>4</sub>) were analyzed on a Seal AA3 Auto-Analyzer. Ammonium was measured with the alkaline phenate method with hypochlorite and sodium nitroprusside (aka Berthelot reaction). The sum of NO<sub>3</sub> + NO<sub>2</sub> were measured following quantitative cadmium coil reduction of NO<sub>3</sub> to NO<sub>2</sub> followed by sulfanilamide reaction in the presence of N-(1-naphthylethylenediamine) dihydrochloride. Errors on

check standards and replicates were less than 5%. DOC and TDN concentrations were analyzed on a Shimadzu TOC- VCSN total organic carbon analyzer, and the coefficient of variance of samples was less than 2% and check standards were accurate within 5%. Dissolved organic nitrogen was calculated as TDN – DIN and used to estimate C/N ratios of the dissolved organic matter.

### Organic matter fluorescence measurements

Fluorescence values, used to evaluate potential organic matter sources and reactivity (Supplementary Table 2), were measured with a Hitachi F-7000 Fluorescence Spectrophotometer to generate 3D Excitation-Emission Matrices (EEMs). Scans were collected at 700 V and at excitation wavelengths ranging from 220–455 nm at 5 nm intervals, and emission wavelengths ranging from 230–600 nm at 2-nm intervals. Instrument-specific effects were corrected for differences in lamp intensity across the excitation-emission wavelength range. Inner filter effects due to organic carbon content were corrected with UV spectra according to methods outlined in Ohno<sup>65</sup>. Aliquots of samples collected for CDOM measurements were used to measure UV absorption at 1 nm intervals from 220–600 nm on a Shimadzu 1800 UV Spectrophotometer. The absorption spectra were used to calculate organic quality parameters including SUVA<sub>254</sub>, BIX, and HIX following methods outlined in Birdwell and Engel<sup>46</sup>. The biological index (BIX) differentiates between freshly produced (autochthonous) and detrital (allochthonous) OM sources and is calculated as the ratio of emission intensities at  $\lambda_{Em} = 380$  nm to  $\lambda_{Em} = 430$  nm at an excitation wavelength of  $\lambda_{Ex} = 310$  nm. Values of BIX between 0.8–1.0 correspond to predominantly autochthonous organic matter, while values of BIX < 0.4 correspond to predominantly allochthonous organic matter (Supplementary Table 2). The humification index (HIX) is positively associated with the age and recalcitrance of organic matter and is calculated as the sum of emission intensities between  $\lambda_{Em} = 435$  nm to  $\lambda_{Em} = 480$  nm divided by the sum of emission intensities between  $\lambda_{Em} = 300$  nm to  $\lambda_{Em} = 345$  nm at an excitation wavelength of  $\lambda_{Ex} = 254$  nm. Values of HIX < 5 are associated with freshly produced organic matter, while greater values (10–30) are associated with predominantly soil organic matter. SUVA<sub>254</sub> values indicate the aromaticity of organic matter by normalizing UV absorbance at 254 nm to the concentration of dissolved organic carbon<sup>66</sup>.

### Weathering model estimates of CO<sub>2</sub> production and consumption

We use a modified mass balance model to evaluate weathering reactions and separate reactions into four categories that include carbonate and silicate mineral weathering by carbonic and sulfuric acid (Supplementary Table 1)<sup>17,31,66</sup>. The model uses major element concentrations of stream water that were corrected for contributions from marine aerosol deposition. The corrections are based on Cl concentrations and assume no mineral contributions to Cl concentrations, which originate solely from marine sources, and that the aerosol deposition has seawater major ion/Cl ratios. The model is based on stoichiometry of four reactions presented in Supplementary Table 1. Separation of carbonate and silicate minerals is based on Ca/Na and Mg/Na molar ratios of bedload sediments, which were taken to be 0.45 and 0.59 respectively (greenmin.g1).

We use the reaction stoichiometry in Supplementary Table 1 to estimate the molar mass balance of the three weathering reactions that impact CO<sub>2</sub> production or consumption. The reactions include carbonic acid dissolution of carbonate and silicate minerals, reported as CA<sub>carb</sub> and CA<sub>sil</sub>, respectively and sulfuric acid dissolution of carbonate minerals SA<sub>carb</sub>. Sulfuric acid dissolution of silicate minerals (SA<sub>sil</sub>) is calculated to complete the mass balance model but has no impact on potential greenhouse gas budgets (Eq. 1).

The standard deviation for the net atmospheric exchange (CO<sub>2eq(ex)</sub>) is given by:

$$\sigma_{net} = \sqrt{(\sigma_1^2 + \sigma_2^2 + \dots + \sigma_n^2)} \quad (2)$$

based on the standard deviations for each average instantaneous watershed exchange estimate calculated per sampling period, where  $\sigma_1$  through  $\sigma_n$  represent the standard deviations of each solute export for each sampling period, calculated as the standard deviation of instantaneous exports calculated for each sampling time. The standard deviations are shown as error bars on Fig. 4b.

### Statistical evaluations

The differences in stream discharge, hydroclimatic variables, and water composition between Periods 1 and 2 were evaluated using Student's *t*-tests. Assumptions included approximately normal distributions and homogeneity of variance. For Period 1,  $n = 14$  and for Period 2  $n = 15$ .

### Data availability

Data used for this paper include geochemical compositions of water samples, stream discharge, hydroclimatic variables, and water and sediment strontium isotopic ratios. Data can be accessed through the Arctic Data Center at <https://arcticdata.io/catalog/view/doi:10.18739/A2ZK55P2M>.

Received: 17 July 2024; Accepted: 20 May 2025;

Published online: 31 May 2025

### References

1. Lambeck, K., Rouby, H., Purcell, A., Sun, Y. & Cambridge, M. Sea level and global ice volumes from the Last Glacial Maximum to the Holocene. *Proc. Natl. Acad. Sci. USA* **111**, 15296–15303 (2014).
2. Martin, J. B., Pain, A. J. & Martin, E. E. Geochemistry of glacial, proglacial, and deglaciated environments. in *Treatise on Geochemistry* 3 251–299 (Elsevier, 2025).
3. Ryder, J. The stratigraphy and morphology of paraglacial alluvial fans in south-central British Columbia. *Can. J. Earth Sci.* **8**, 279–298 (1971).
4. Ballantyne, C. K. A general model of paraglacial landscape response. *Holocene* **12**, 371–376 (2002).
5. Church, M. & Ryder, J. M. Paraglacial sedimentation: a consideration of fluvial processes conditioned by glaciation. *Geol. Soc. Am. Bull.* **83**, 3059–3072 (1972).
6. Screen, J. A. & Simmonds, I. The central role of diminishing sea ice in recent Arctic temperature amplification. *Nature* **464**, 1334–1337 (2010).
7. Holland, M. M. & Bitz, C. M. Polar amplification of climate change in coupled models. *Clim. Dyn.* **21**, 221–232 (2003).
8. Bekryaev, R. V., Polyakov, I. V. & Alexeev, V. A. Role of polar amplification in long-term surface air temperature variations and modern arctic warming. *J. Clim.* **23**, 3888–3906 (2010).
9. Bamber, J. L., Oppenheimer, M., Kopp, R. E., Aspinall, W. P. & Cooke, R. M. Ice sheet contributions to future sea-level rise from structured expert judgment. *Proc. Natl. Acad. Sci. USA* **166**, 11195–11200 (2019).
10. Bamber, J., Van Den Broeke, M., Ettema, J., Lenaerts, J. & Rignot, E. Recent large increases in freshwater fluxes from Greenland into the North Atlantic. *Geophys. Res. Lett.* **39**, L19501 (2012).
11. Bhatia, M. P. et al. Greenland meltwater as a significant and potentially bioavailable source of iron to the ocean. *Nat. Geosci.* **6**, 274–278 (2013).
12. Bhatia, M. P. et al. Organic carbon export from the Greenland ice sheet. *Geochim Cosmochim. Acta* **109**, 329–344 (2013).
13. Hawkers, J. R. et al. Ice sheets as a missing source of silica to the polar oceans. *Nat. Commun.* **8**, 14198 (2017).
14. Wadham, J. L. et al. Ice sheets matter for the global carbon cycle. *Nat. Commun.* **10**, 3567 (2019).
15. Hawkers, J. et al. The Greenland Ice Sheet as a hot spot of phosphorus weathering and export in the Arctic. *Glob. Biogeochem. Cycles* **30**, 191–210 (2016).
16. Hawkers, J. R. et al. Enhanced trace element mobilization by Earth's ice sheets. <https://doi.org/10.1073/pnas.2014378117/-DCSupplemental>.

17. Deuerling, K. M. et al. Chemical weathering across the western foreland of the Greenland Ice Sheet. *Geochim Cosmochim. Acta* **245**, 426–440 (2019).
18. Martin, J. B., Pain, A. J., Martin, E. E., Rahman, S. & Ackerman, P. Comparisons of Nutrients Exported From Greenlandic Glacial and Deglaciated Watersheds. *Global Biogeochem Cycles* **34**, e2020GB006661 (2020).
19. Holmes, R. M. et al. Seasonal and Annual Fluxes of Nutrients and Organic Matter from Large Rivers to the Arctic Ocean and Surrounding Seas. *Estuaries Coasts* **35**, 369–382 (2012).
20. Terhaar, J., Lauerwald, R., Regnier, P., Gruber, N. & Bopp, L. Around one third of current Arctic Ocean primary production sustained by rivers and coastal erosion. *Nat. Commun.* **12**, 169 (2021).
21. Connolly, C. T. et al. Watershed slope as a predictor of fluvial dissolved organic matter and nitrate concentrations across geographical space and catchment size in the Arctic. *Environ. Res. Lett.* **13**, 104015 (2018).
22. Martin, J. B. Carbonate minerals in the global carbon cycle. *Chem. Geol.* **449**, 58–72 (2017).
23. Torres, M. A., West, A. J. & Li, G. Sulphide oxidation and carbonate dissolution as a source of CO<sub>2</sub> over geological timescales. *Nature* **507**, 346–349 (2014).
24. Walker, J. C. G., Hays, P. B. & Kasting, J. F. A negative feedback mechanism for the long-term stabilization of Earth's surface temperature. *J. Geophys. Res.* **86**, 9776–9782 (1981).
25. Berner, R. A., Lasaga, A. C. & Garrels, R. M. The carbonate-silicate geochemical cycle and its effect on atmospheric carbon dioxide over the past 100 million years. *Am. J. Sci.* **283**, 641–683 (1983).
26. Mar, K. A., Unger, C., Walderdorff, L. & Butler, T. Beyond CO<sub>2</sub> equivalence: The impacts of methane on climate, ecosystems, and health. *Environ. Sci. Policy* **134**, 127–136 (2022).
27. Pain, A. J., Martin, J. B., Martin, E. E., Rahman, S. & Ackermann, P. Differences in the Quantity and Quality of Organic Matter Exported From Greenlandic Glacial and Deglaciated Watersheds. *Global Biogeochem. Cycles* **34**, e2020GB006614 (2020).
28. Bradley-Cook, J. I. & Virginia, R. A. Landscape variation in soil carbon stocks and respiration in an Arctic tundra ecosystem, west Greenland. *Arct. Antarct. Alp. Res.* **50**, e1420283 (2018).
29. Bradley-Cook, J. I. & Virginia, R. A. Soil carbon storage, respiration potential, and organic matter quality across an age and climate gradient in southwestern Greenland. *Polar Biol.* **39**, 1283–1295 (2016).
30. Rocher-Ros, G. et al. Metabolism overrides photo-oxidation in CO<sub>2</sub> dynamics of Arctic permafrost streams. *Limnol. Oceanogr.* **66**, S169–S181 (2021).
31. Kling, G. W., Kipphut, G. W. & Miller, M. C. Arctic Lakes and Streams as Gas Conduits to the Atmosphere: Implications for Tundra Carbon Budgets. *Science* **251**, 298–301 (1991).
32. Connolly, C. T., Cardenas, M. B., Burkart, G. A., Spencer, R. G. M. & McClelland, J. W. Groundwater as a major source of dissolved organic matter to Arctic coastal waters. *Nat. Commun.* **11**, 1479 (2020).
33. Wrona, F. J. et al. Transitions in Arctic ecosystems: Ecological implications of a changing hydrological regime. *J. Geophys. Res.: Biogeosciences* **121**, 650–674 (2016).
34. Roberts, K. E. et al. Climate and permafrost effects on the chemistry and ecosystems of High Arctic Lakes. *Sci. Rep.* **7**, 13292 (2017).
35. Scribner, C. A. et al. Exposure age and climate controls on weathering in deglaciated watersheds of western Greenland. *Geochim Cosmochim. Acta* **170**, 157–172 (2015).
36. Hood, E. & Scott, D. Riverine organic matter and nutrients in southeast Alaska affected by glacial coverage. *Nat. Geosci.* **1**, 583–587 (2008).
37. Göransson, H., Welc, M., Bünenmann, E. K., Christl, I. & Venterink, H. O. Nitrogen and phosphorus availability at early stages of soil development in the Damma glacier forefield, Switzerland; implications for establishment of N<sub>2</sub>-fixing plants. *Plant Soil* **404**, 251–261 (2016).
38. Yoshitake, S., Uchida, M., Iimura, Y., Ohtsuka, T. & Nakatsubo, T. Soil microbial succession along a chronosequence on a High Arctic glacier foreland, Ny-Ålesund, Svalbard: 10 years' change. *Polar Sci.* **16**, 59–67 (2018).
39. Norton, S. A. et al. The controls on phosphorus availability in a Boreal lake ecosystem since deglaciation. *J. Paleolimnol.* **46**, 107–122 (2011).
40. Larsen, N. K. et al. Rapid early Holocene ice retreat in West Greenland. *Quat. Sci. Rev.* **92**, 310–323 (2014).
41. Kottek, M., Grieser, J., Beck, C., Rudolf, B. & Rubel, F. World map of the Köppen-Geiger climate classification updated. *Meteorologische Z.* **15**, 259–263 (2006).
42. Lenaerts, J. T. M. et al. Representing Greenland ice sheet freshwater fluxes in climate models. *Geophys Res Lett.* **42**, 6373–6381 (2015).
43. Rudd, D. A., Karami, M. & Fensholt, R. Towards high-resolution land-cover classification of greenland: A case study covering Kobbefjord, Disko and Zackenberg. *Remote Sens. (Basel)* **13**, 3559 (2021).
44. Larsen, N. K. et al. Strong altitudinal control on the response of local glaciers to Holocene climate change in southwest Greenland. *Quat. Sci. Rev.* **168**, 69–78 (2017).
45. Abermann, J., Langley, K., Myreng, S. M., Rasmussen, K. & Petersen, D. Heterogeneous timing of freshwater input into Kobbefjord, a low-arctic fjord in Greenland. *Hydro. Process* **35**, e14413 (2021).
46. Birdwell, J. E. & Engel, A. S. Characterization of dissolved organic matter in cave and spring waters using UV-Vis absorbance and fluorescence spectroscopy. *Org. Geochem* **41**, 270–280 (2010).
47. Pain, A. J., Martin, J. B., Martin, E. E., Rennermalm, Å. K. & Rahman, S. Heterogeneous CO<sub>2</sub> and CH<sub>4</sub> content of glacial meltwater from the Greenland Ice Sheet and implications for subglacial carbon processes. *Cryosphere* **15**, 1627–1644 (2021).
48. Lamhonwah, D., Lafrenière, M. J., Lamoureux, S. F. & Wolfe, B. B. Evaluating the hydrological and hydrochemical responses of a High Arctic catchment during an exceptionally warm summer. *Hydro. Process* **31**, 2296–2313 (2017).
49. Shogren, A. J. et al. Arctic concentration–discharge relationships for dissolved organic carbon and nitrate vary with landscape and season. *Limnol. Oceanogr.* **66**, S197–S215 (2021).
50. Paulsen, M. L. et al. Carbon Bioavailability in a High Arctic Fjord Influenced by Glacial Meltwater, NE Greenland. *Front Mar. Sci.* **4**, 1–19 (2017).
51. Lamarche-Gagnon, G. et al. Greenland melt drives continuous export of methane from the ice-sheet bed. *Nature* **565**, 73–77 (2019).
52. Chiasson-Poirier, G., Franssen, J., Lafrenière, M. J., Fortier, D. & Lamoureux, S. F. Seasonal evolution of active layer thaw depth and hillslope-stream connectivity in a permafrost watershed. *Water Resour. Res.* **56**, e2019WR025828 (2020).
53. Hirst, C. et al. Evidence for late winter biogeochemical connectivity in permafrost soils. *Commun. Earth Environ.* **4**, 85 (2023).
54. St Pierre, K. A. et al. Proglacial freshwaters are significant and previously unrecognized sinks of atmospheric CO<sub>2</sub>. *Proc. Natl. Acad. Sci. USA* **116**, 17690–17695 (2019).
55. Shogren, A. J., Zarnetske, J. P., Abbott, B. W., Iannucci, F. & Bowden, W. B. We cannot shrug off the shoulder seasons: Addressing knowledge and data gaps in an Arctic headwater. *Environ. Res. Lett.* **15**, 104027 (2020).
56. Hartmann, J., Jansen, N., Dürr, H. H., Kempe, S. & Köhler, P. Global CO<sub>2</sub>-consumption by chemical weathering: What is the contribution of highly active weathering regions?. *Glob. Planet Change* **69**, 185–194 (2009).
57. Parker, R. L. et al. Laurentide Ice Sheet extent over the last 130 thousand years traced by the Pb isotope signature of weathering inputs to the Labrador Sea. *Quat. Sci. Rev.* **287**, 107564 (2022).
58. Crocket, K. C., Vance, D., Foster, G. L., Richards, D. A. & Tranter, M. Continental weathering fluxes during the last glacial/interglacial cycle:

Insights from the marine sedimentary Pb isotope record at Orphan Knoll, NW Atlantic. *Quat. Sci. Rev.* **38**, 89–99 (2012).

59. Bohm, E. et al. Strong and deep Atlantic meridional overturning circulation during the last glacial cycle. *Nature* **517**, 73–76 (2015).

60. Colosimo, P. F. et al. Widespread parallel evolution in sticklebacks by repeated fixation of ectodysplasin alleles. *Science* ((1979)) **307**, 1928–1933 (2005).

61. Frank, M. Radiogenic isotopes: Tracers of past ocean circulation and erosional input. *Rev. Geophys.* **40**, 1-1–1–38 (2002).

62. Repo, M. E. et al. Release of CO<sub>2</sub> and CH<sub>4</sub> from small wetland lakes in western Siberia. *Tellus B Chem. Phys. Meteorol.* **59**, 788–796 (2007).

63. Pain, A. J., Martin, J. B. & Young, C. R. Sources and sinks of CO<sub>2</sub> and CH<sub>4</sub> in siliciclastic subterranean estuaries. *Limnol. Oceanogr.* **64**, 1500–1514 (2019).

64. Pin, C. & Bassin, C. Evaluation of a strontium-specific extraction chromatographic method for isotopic analysis in geological materials. *Anal. Chim. Acta* **269**, 249–255 (1992).

65. Ohno, T. Fluorescence inner-filtering correction for determining the humification index of dissolved organic matter. *Environ. Sci. Technol.* **36**, 742–746 (2002).

66. Weishaar, J. L. et al. Evaluation of Specific Ultraviolet Absorbance as an Indicator of the Chemical Composition and Reactivity of Dissolved Organic Carbon. *Environ. Sci. Technol.* **37**, 4702–4708 (2003).

## Acknowledgements

A.J.P., J.B.M., and E.E.M. acknowledge support for this research from INTERACT (International Network for Terrestrial Research and Monitoring in the Arctic). J.M.B. and E.E.M. also acknowledge support for the research related to this work from the US National Science Foundation [Grant number 2000649]. A.J.P., J.B.M., and E.E.M. thank Katrine Raundrup for logistical help and coordination in the field and at the Greenland Institute of Natural Resources (GINR). Authors are grateful for reviewer suggestions that greatly enhanced the manuscript. No visas, import, or export licenses were needed for transport of equipment or samples.

## Author contributions

A.J.P., J.B.M., and E.E.M. designed the study and carried out the field work, A.J.P. conducted solutes, water isotope, and gas analyses and mass balance modeling, JTS-R and CB conducted Sr isotope analyses, A.J.P. and

J.B.M. co-wrote the initial manuscript and all authors contributed to data analyses and manuscript editing.

## Competing interests

The authors declare no competing interests.

## Additional information

**Supplementary information** The online version contains supplementary material available at <https://doi.org/10.1038/s43247-025-02404-z>.

**Correspondence** and requests for materials should be addressed to A. J. Pain.

**Peer review information** *Communications Earth & Environment* thanks and the other, anonymous, reviewer(s) for their contribution to the peer review of this work. Primary handling editors Somaparna Ghosh. A peer review file is available.

**Reprints and permissions information** is available at <http://www.nature.com/reprints>

**Publisher's note** Springer Nature remains neutral with regard to jurisdictional claims in published maps and institutional affiliations.

**Open Access** This article is licensed under a Creative Commons Attribution 4.0 International License, which permits use, sharing, adaptation, distribution and reproduction in any medium or format, as long as you give appropriate credit to the original author(s) and the source, provide a link to the Creative Commons licence, and indicate if changes were made. The images or other third party material in this article are included in the article's Creative Commons licence, unless indicated otherwise in a credit line to the material. If material is not included in the article's Creative Commons licence and your intended use is not permitted by statutory regulation or exceeds the permitted use, you will need to obtain permission directly from the copyright holder. To view a copy of this licence, visit <http://creativecommons.org/licenses/by/4.0/>.

© The Author(s) 2025